
IMPROVED CRYO-EM POSE ESTIMATION AND 3D CLASSIFICATION THROUGH LATENT-SPACE DISENTANGLEMENT

Weijie Chen^{a,b}, Yuhang Wang^{a*}, and Lin Yao^{a**}

^a DP Technology, Ltd., Beijing, China; ^b Peking University, Beijing, China
baoz@pku.edu.cn, stevenwaura@gmail.com, yaol@dp.tech

ABSTRACT

Due to the extremely low signal-to-noise ratio (SNR) and unknown poses (projection angles and image shifts) in cryo-electron microscopy (cryo-EM) experiments, reconstructing 3D volumes from 2D images is very challenging. In addition to these challenges, heterogeneous cryo-EM reconstruction requires conformational classification. In popular cryo-EM reconstruction algorithms, poses and conformation classification labels must be predicted for every input cryo-EM image, which can be computationally costly for large datasets. An emerging class of methods adopted the amortized inference approach. In these methods, only a subset of the input dataset is needed to train neural networks for the estimation of poses and conformations. Once trained, these neural networks can make pose/conformation predictions and 3D reconstructions at low cost for the entire dataset during inference. Unfortunately, when facing heterogeneous reconstruction tasks, it is hard for current amortized-inference-based methods to effectively estimate the conformational distribution and poses from entangled latent variables. Here, we propose a self-supervised variational autoencoder architecture called “HetACUMN” based on amortized inference. We employed an auxiliary conditional pose prediction task by inverting the order of encoder-decoder to explicitly enforce the disentanglement of conformation and pose predictions. Results on simulated datasets show that HetACUMN generated more accurate conformational classifications than other amortized or non-amortized methods. Furthermore, we show that HetACUMN is capable of performing heterogeneous 3D reconstructions of a real experimental dataset.

1 Introduction

Cryo-electron microscopy (cryo-EM) is an experimental method for resolving the structures of 3-dimensional (3D) objects (typically biological molecules) from 2-dimensional (2D) projection images. This technique has seen rapid progress in the past decade. The 3D structures of many important biological molecules have been resolved based on this method, such as the SARS-Cov-2 relevant proteins [29]. Recognizing its importance, the 2017 Nobel prize in chemistry was awarded to the three pioneers of cryo-EM [12].

There are three challenging aspects of cryo-EM reconstructions that are different from 3D reconstructions from natural images commonly seen in computer vision area. First, the signal-to-noise ratio (SNR) of cryo-EM images is very low (around -10 dB), making it hard to distinguish signals from noise. The distribution of noise is also complex. It can vary significantly between various datasets due to different experimental conditions and the nature of target sample objects. The second challenge is to recover the projection angle and 2D image translations (collectively termed “poses”) from images alone. The quality of final reconstructed objects depends the accuracy of the estimation of pose. In single-particle cryo-EM, the pose information is completely missing during experimental measurements, and can only be estimated based on a large set of projections. On top of these two challenges, the cryo-EM 3D reconstruction problem is further compounded by the fact that the underlying objects exist in many possible conformations. Here the conformations refer to various possible shapes of the same molecule (e.g., a protein), akin to different postures of a human body. Heterogeneous cryo-EM 3D reconstruction is concerned with solving all three challenges, which is a difficult and heavily researched direction [1].

*Corresponding authors

Recent advances in deep learning and computer vision provided new paths for solving these challenges, as have been demonstrated in previous work such as cryoDRGN2 [33] and cryoFIRE [9]. CryoDRGN2 can generate accurate classifications and reconstructions of heterogeneous EM datasets [33], but the computational cost is high for large datasets [9]. CryoFIRE demonstrated significant speed-up compared to CryoDRGN2, but at the cost of reduced accuracy [9]. To overcome these problems, here we propose a new method called HetACUMN (Heterogeneous reconstruction with Amortized Classification Using Multi-task Networks) with the following highlights.

- We propose a novel training framework for enforcing disentanglement of pose and conformation, which is specifically designed for heterogeneous reconstructions.
- We demonstrate the effectiveness of our method on simulated datasets, achieving high-quality reconstructions and better performance of conformational classification.
- Our method can also be applied for heterogeneous reconstruction of experimental datasets, demonstrating its value in protein structure studies.

2 Background

In cryo-EM, a large number of macromolecules are frozen with random orientation and independent conformations in a thin layer of vitreous ice. Probing electrons interact with electrostatic potential created by these molecules and produce two-dimensional tomographic projection images. The volumes $\{V_i\}_{i=1,\dots,N}$ can be assumed as a subset of conformations independently sampled from the conformational space of macromolecules. It is assumed that conformational space \mathcal{M} can be characterized by a low-dimension manifold and embedded in \mathbb{R}^d .

On the screen of observer, each molecule is in unknown orientation $R_i \in SO(3) \subset \mathbb{R}^{3 \times 3}$ and conformational state $z_i \in \mathbb{R}^d$. The electron beam interacts with the molecules and projects a 2D image \mathcal{I}_i . Besides, the system’s impulse response can be represented by the Point Spread Function (PSF) P_i , which can be estimated based on microscope imaging parameters. More specifically, each image can be modeled as follows:

$$\mathcal{I}_i(x, y) = T_{t_i} * P_i * \int_{\omega} V(R_i \cdot [x, y, \omega]^T, z_i) d\omega + \epsilon_i \tag{1}$$

where $*$ is the convolution operation, T_t is the translation operator characterized by $t \in \mathbb{R}^2$, ϵ_i is noise.

Based on the Fourier slice theorem [23], we can bypass the computation of integrals and convolutions in Eq. (1).

$$\mathcal{F}_{2D}[\int_{\omega} V(R_i^T \cdot [x, y, \omega], z_i) d\omega] = \mathcal{F}_{3D}[V](R_i^T \cdot [k_x, k_y, 0], z_i) \tag{2}$$

where \mathcal{F}_{2D} and \mathcal{F}_{3D} denote 2D and 3D Fourier transform respectively. Finally, Eq. (1) can be rewritten with Fourier transform $\hat{\mathcal{I}} = \mathcal{F}_{2D}[\mathcal{I}]$ and $\hat{V} = \mathcal{F}_{3D}[V]$:

$$\hat{\mathcal{I}}_i(k_x, k_y) = \hat{T}_{t_i} \odot C_i \odot \hat{V}(R_i^T \cdot [k_x, k_y, 0], z_i) + \hat{\epsilon}_i \tag{3}$$

where \odot is element-wise multiplication, $C_i = \mathcal{F}_{2D}[P_i]$ is the Contrast Transfer Function (CTF) [10], \hat{T}_t is the translation operator in Fourier space.

3 Related Work

Here we review existing methods relevant to heterogeneous cryo-EM reconstructions.

3.1 Conformational classification

In traditional cryo-EM software such as RELION [20] and cryoSPARC [17], conformational heterogeneity is usually modeled as a set of discrete conformations for simplicity using expectation-maximization-based algorithms. Alternatively, the heterogeneity can be represented continuously. One class of such methods use deformation-based approaches, such as rigid bodies[21], normal-mode-based eigenvolumes [4], 3D linear subspace models [16], deformation field [6, 15] and high-dimensional molecules (“hyper-molecules”) [7]. Another class uses a neural-network-based representation to encode conformational variability implicitly into network parameters, which include cryoDRGN-BNB [32], cryoDRGN2 [33], and cryoFIRE [9]. This line of approach doesn’t require any prior knowledge or initial guesses of the conformational distribution as used in the deformation-based methods, and is therefore less biased. HetACUMN also adopted this approach.

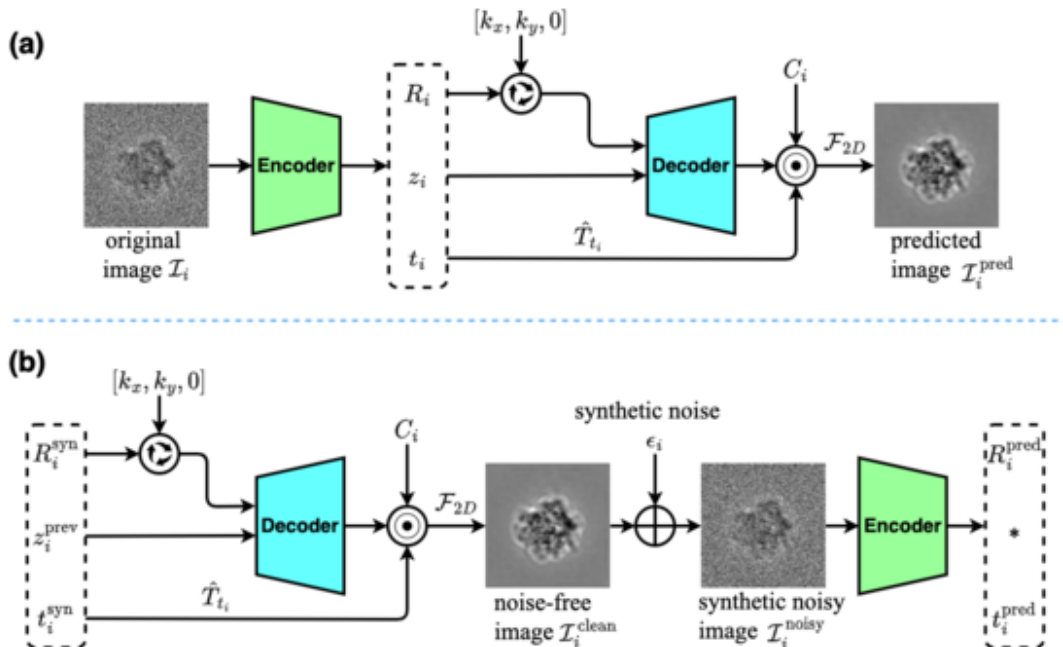


Figure 1: Architectures of the two tasks in HetACUMN. **(a)** the variational image reconstruction task; **(b)** the conditional pose prediction (CPP) task.

3.2 Pose estimation

Pose estimation refers to estimating projection angles and image translations (collectively termed as “poses”) only from 2-dimensional (2D) cryo-EM projection images. It is one of the hardest problems in cryo-EM, especially in heterogeneous cryo-EM reconstruction.

In the majority of literature, pose estimation is performed on a per-image basis under the expectation-maximization framework, including RELION[21], cryoSPARC[17], 3DFlex[15], cryoDRGN-BNB[32], cryoDRGN2[33], and cryoFold[22]. Although these methods can usually reach good accuracy, the associated computational cost is significant for large datasets. (see [1] for an up-to-date in-depth review). There has also been attempts to bypass the pose estimation problem through the generative adversarial network as implemented in cryoGAN [3], but the reconstruction resolution is inferior to other methods.

To reduce the computational cost while maintaining high reconstruction quality, recent development focused on an alternative approach called amortized inference. In this approach, the pose estimation problem is formulated as optimizing the parameters ξ of a function $f_\xi(\mathcal{I}) = (R, t)$ that maps an input image \mathcal{I} to its associated rotation R and translation t . Earlier attempts of amortized-inference-based methods have limited accuracy, e.g., FSTDiff [25] and CryoPoseNet [11]. CryoAI [8] showed that amortized-inference-based methods can easily get trapped in local minima which leads to spurious planar symmetry. To overcome this drawback, CryoAI proposed to use symmetrized loss (see Methods section for details) and reached pose estimation accuracy on par with non-amortized methods. ACE-EM [28] proposed a dual-task training framework to improve the accuracy of pose estimation. Besides the usual self-supervised learning for image reconstruction, they designed an extra supervised learning for pose prediction.

3.3 Joint estimation of conformations and poses

AtomVAE [19] is one of the early attempts to use amortized-inference-based joint estimation based on the VAE architecture, which showed promising results on simulated datasets. It discussed several key observations such as the importance of disentangling the conformational latent space and pose latent space and the pre-training of the pose prediction using the fixed base structure. More recently, combining cryoDRGN and cryoAI’s architectures, cryoFIRE [9] demonstrated that it is possible to obtain good reconstruction quality using joint amortized inferences on both simulated and experimental datasets. In cryoFIRE, input images are fed into a Convolutional Neural Network (CNN) to extract visual features. Then, through three multi-layer perceptrons (MLP), the pose parameters (i.e., orientation R and translation t) and image classification labels (i.e., conformation z) are estimated from the visual features. They propose

a ‘‘pose-only phase’’ to enable the model to converge to a consensus volume. They disable the optimization of the conformation MLP at the early stage of training and sample from a normalized Gaussian distribution. Here, we show that this strategy is not sufficient to disentangling conformational latent space and pose latent space. Inspired by ACE-EM [28], we proposed a conditional supervised pose learning task for the joint pose-conformation estimation and achieved state-of-the-art performance on different heterogeneous datasets.

4 Methods

4.1 Overview of HetACUMN

HetACUMN consists of two tasks (Figure 1). One task is for variational image reconstruction. Raw EM images \mathcal{I}_i are fed into an encoder for predicting three latent variables: orientation R_i , image shift t_i , and conformational state z_i . The decoder acts as a physics-based simulator of cryo-EM image projection to represent the Fourier volume \hat{V} . It takes the predicted conformational state and the grid of L^2 3D-coordinates rotated by estimated rotation, then outputs the corresponding projection images. With the estimated translation and the given CTF parameters C_i , the projection images are post-processed to obtain a noise-free reconstruction of input images.

The second task is for conditional pose prediction (CPP), which exploits the same encoder-decoder as the first task but in reversed order to explore larger pose spaces. Instead of image reconstruction, it reconstructs the corresponding projection poses from randomly sampled poses with the reversed pipeline, and minimizes the difference between the pose pairs, i.e., conditional pose prediction task.

In this method, we can balance the pose estimation and image reconstruction by alternating two tasks to optimize the VAE-based model during training.

4.2 Variational image reconstruction task

The variational image reconstruction task follows the standard self-supervised learning with the usual encoder-decoder order. The main objective of variational image reconstruction task is to minimize the difference between the input images and predicted images. Assuming the image length of L , mean squared error (MSE) loss function is often used to measure their gap.

$$\mathcal{L}_{\text{image}}(\mathcal{I}_i) = \frac{1}{L^2} \|\mathcal{I}_i - \mathcal{I}_i^{\text{pred}}\|_F^2 \quad (4)$$

where $\|A\|_F = \sqrt{\sum_{i,j} |A_{i,j}|^2}$ is the Frobenius norm.

To reduce the chance of reconstructing volumes with the spurious pseudo-mirror symmetry artefact, we followed added a slighted modified version of the *symmetrized loss* proposed by cryoAI [8]:

$$\mathcal{L}_{\text{sym}} = \min\{\mathcal{L}_{\text{image}}(\mathcal{I}_i), \mathcal{L}_{\text{image}}(\mathcal{R}_h[\mathcal{I}_i])\} \quad (5)$$

where \mathcal{R}_h represents horizontal image flipping.

For conformational state, the conformation head of encoder predicts mean $\mu_{z|\mathcal{I}} \in \mathbb{R}^d$ and variance $\sigma_{z|\mathcal{I}}^2 \in \mathbb{R}_+^d$ for each image, as the variational approximation to the posterior $q(z|\mathcal{I})$. In general, the prior $p(z)$ on the conformational space is a standard Gaussian distribution. We introduce Kullback-Leibler (KL) divergence for optimizing posterior distribution.

$$\mathcal{L}_z = D_{KL}(q(z|\mathcal{I}_i) \| p(z)) \quad (6)$$

At the early stage of training, we sample the conformational states from the prior distribution and freeze the training of conformation head to focus on improving pose estimation alone.

Besides, we added an L1-regularization for predicted translation to prevent unrealistic large shift and keep the reconstructed object near the center of the coordinate grid as much as possible. The total loss of variational image reconstruction task as follows:

$$\mathcal{L}_I = \mathcal{L}_{\text{sym}} + \lambda_z \mathcal{L}_z + \lambda_t \frac{1}{2} \|t_i^{\text{pred}}\|_1 \quad (7)$$

where $\lambda_z = 1 \times 10^{-4}$, $\lambda_t = 1 \times 10^{-3}$

4.3 Conditional pose prediction task

The conditional pose prediction task takes the encoder and decoder from the multi-class image reconstruction task and reversed order. Compared to the variational image reconstruction task, the inputs and ground-truth labels are

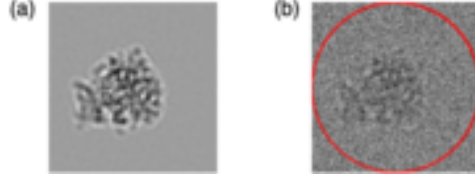


Figure 2: Example of noisy EM image generation. **(a)** a noise-free reconstructed image. **(b)** a synthetic noisy EM image with SNR = -10 dB. The area outside the red circle is considered as the noise-only region.

no long EM images, but poses uniformly sampled over over $SO(3) \times \mathbb{R}^2$. This encoder-decoder order reversal turns the decoder into a EM image data generator conditioned on a particular conformation. It also exposes the latent pose variables for direct supervised learning. In this task, the conformational states are sampled from the posterior distribution of the previous multi-class image reconstruction task. The conformational states z_i^{prev} and sampled poses are fed into the decoder (parameters frozen) to generate noise-free images $\mathcal{I}_i^{\text{clean}}$. To generate more realistic inputs for the encoder, the additive noise estimated from the input datasets is added to the predicted noise-free images. Then, the encoder E_θ takes the synthetic noisy images and predict the poses.

We define the conditional pose estimation loss function as follows, where $\lambda_p = 0.1$.

$$\mathcal{L} = \lambda_p \left[\frac{1}{9} \|R_i^{\text{syn}} - R_i^{\text{pred}}\|_F^2 + \frac{1}{2} \|t_i^{\text{syn}} - t_i^{\text{pred}}\|_1 \right] \quad (8)$$

This task can also be viewed as a data-augmentation technique. Therefore, the encoder can learn from a comprehensive pose training datasets even if the input EM image dataset is small or has highly biased pose distribution.

4.3.1 Noise Generation

In cryo-EM images, the noise is often simplified as being additive independent, zero-mean Gaussian noise [21, 26]. One can estimate the variance of noise from the corners of the EM images and add synthetic noise to noise-free images directly (Figure 2). However, due to low SNR, this method will overwhelm the detail of images and mislead the encoder in early training.

In our work, we proposed an adaptive noise generation method that generates noise with the fixed SNR instead of using a fixed variance of noise. In other words, the intensity of synthetic noise will increase as the detail of the image reconstruction enhances. Assuming that the distributions of noise and image signals are independent, we can estimate the SNR of datasets by following:

$$\text{SNR} \triangleq \frac{\sigma_{\mathcal{I}^{\text{clean}}}^2}{\sigma_\epsilon^2} = \frac{\sigma_{\mathcal{I}}^2 - \sigma_\epsilon^2}{\sigma_\epsilon^2} \quad (9)$$

where σ_ϵ^2 is the variance of noise and $\sigma_{\mathcal{I}}^2$ is the variance of noisy images. During training, the noise can be generated from the following Gaussian distribution.

$$\epsilon_k \sim \mathcal{N}(0, \sigma_{\epsilon_k}^2) \text{ where } \sigma_{\epsilon_k}^2 = \sigma_{\mathcal{I}^{\text{clean},k}}^2 / \text{SNR} \quad (10)$$

where ϵ_k is the synthesized noise at the k -th step, $\mathcal{I}^{\text{clean},k}$ is the reconstructed noise-free images at the k -th step.

4.4 Metric for measuring latent-space entanglement

Currently there are no commonly accepted metrics for measuring the latent-space entanglement for deep-learning-based heterogeneous cryo-EM reconstruction algorithms. In cryo-EM, poses and conformations have real physical meanings. Thus, we propose to measure the entanglement between poses and conformations as $E_{\text{entangle}} = \mathcal{E}_{\text{pose}} + \mathcal{E}_z$, where $\mathcal{E}_{\text{pose}}$ and \mathcal{E}_z are pose and conformation label z prediction errors, respectively. Lower entanglement values indicate better disentanglement. The pose error $\mathcal{E}_{\text{pose}} = \mathcal{E}_{\text{rot}} + \mathcal{E}_{\text{trans}}$. The generalized classification error \mathcal{E}_z of multi-classification can be measured using the mean (μ_i) and standard deviation (σ_i) of each class (Eq. 11). N_{pair} is the number of unique pairs.

$$\mathcal{E}_z = \frac{1}{N_{\text{pair}}} \sum_{i < j} \exp \left(-\frac{(\mu_i - \mu_j)^2}{\sigma_i \sigma_j} \right) \quad (11)$$

5 Experiments

5.1 Reconstructions on Simulated Datasets

Experimental Setup

To evaluate our method against ground truth values and other methods, we created two simulated heterogeneous cryo-EM datasets to quantitatively and qualitatively assess the performance of HetACUMN (more details see supplementary material).

In the first dataset (termed “**80S-bimodal**” hereafter), two ground-truth volumes were taken from a published dataset [30, 31], which correspond to the rotated and unrotated states of the 80S ribosome protein. We created two simulated datasets with 20k/100k images (image size $D = 128$; $3.77 \text{ \AA}/\text{pixel}$) using the cryo-EM image formation model, with an equal number of projection images for these two ground-truth volumes.

Projection angles were sampled uniformly from the 3D rotation group $SO(3)$. 2D image translations were sampled from a uniform distribution between $[-8, 8]$ pixels along X and Y axes. Gaussian noise was added to reach a signal-to-noise ratio (SNR) of -10 dB. CTF parameters were taken from an experimental dataset EMPIAR-10028 [27].

The second dataset (termed “**1D-motion**”) contains 100k images. It was generated from a 1-dimensional (1D) rigid-body rotational motion of a protein fragment. We chose 10 representative states to generate the ground truth volumes. Projection images (image size $D = 64$; $3.0 \text{ \AA}/\text{pixel}$) were generated in the same way as the “80S-bimodal” dataset.

We trained HetACUMN with the dimension of the latent variable z set to 8 and activated the update of conformational states after 50 epochs. The ADAM optimizer with learning rate of 1.5×10^{-4} was used to optimize our model. The size of batches is set to 128 and 512 respectively for the two datasets. cryoDRGN2 [33] was trained with its default parameters. The size of batches was set to 24 and 48 respectively for the two datasets. cryoFIRE [9] was also trained with its default settings. To better comparison with ours, we set the same size of training batches and activate the conformation MLP after the same epochs. We trained all of the methods on a single NVIDIA V100 32GB.

For visualization, we use principle component analysis (PCA) to transform conformational state z_i into principle components (PC). After convergence, we generate 3D volumes by taking the centroids of the clusters in the reduced principle component space and inverse-transform them into the corresponding z_i values.

Benchmark on the 80S-bimodal datasets

With 80S-bimodal datasets, we compare HetACUMN with cryoDRGN2 [33] and cryoFIRE [9], and evaluate the performance of heterogeneous reconstruction from the following metrics:

- Rot.: the median squared error of rotation matrices using the Frobenius norm.
- Trans.: the median squared error of the predicted translation vectors (in pixels).
- Res.: the FSC resolution (in pixels) is the inverse of the spatial frequency corresponding to a Fourier Shell Correlation (FSC) coefficient of 0.5 between the predicted and ground-truth volumes.
- Err.: the percentage of mis-classified images over the total number of images

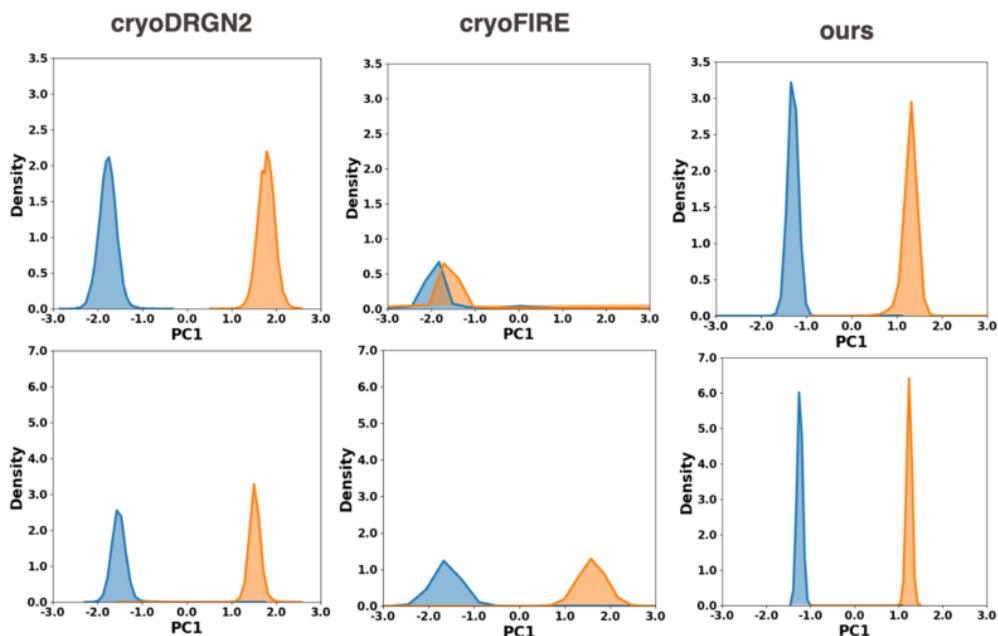
The performance of the three methods on the 80S bimodal datasets is presented in Table 1 as well as Figure 3 and 4. CryoDRGN2 [33] performed well on both the 20k and 100k datasets thanks to the less scalable but more accurate exhaustive pose search technique. CryoFIRE, an amortized inference method, performed poorly on the 20k dataset but its performance improved greatly when the dataset size increased to 100k. HetACUMN, also based on amortized inference, outperformed cryoFIRE in all metrics, and achieved comparable pose estimation accuracy as cryoDRGN2.

Among all metrics, the classification error is the most important one, which indicates the ability of the model to distinguish different conformations. For the small dataset (20k), cryoDRGN2 correctly classified all images. CryoFIRE, on the other hand, mis-predicted the classification labels for a large portion of the dataset (38%). HetACUMN performed comparable to cryoDRGN2 and only mis-classified two images (0.01%). When the dataset size was increased to 100k, cryoDRGN2’s classification error increased to 0.07%. CryoFIRE’s performance on this larger dataset was slightly better than cryoDRGN2 (0.02%). HetACUMN outperformed both cryoDRGN2 and cryoFIRE and reduced the classification error to 0.009%. The poor performance of cryoFIRE on the smaller dataset (20k) indicates a severe limitation of this method. We argue that this is not an inherent drawback of amortized inference. HetACUMN is a better alternative when the data and/or computational resource is limited, which performed well on both small and large datasets.

Aside from these metrics, an interesting observation from Figure 3 is that the latent- z space of HetACUMN (after dimension reduction) showed much more concentrated distributions than cryoDRGN2 and cryoFIRE. As the number

Table 1: Benchmark results for the 80S bimodal datasets. The best results are highlighted in bold. FSC resolutions are listed for both volumes.

Methods	cryoDRGN2 (non-amortized)	cryoFIRE (amortized)	HetACUMN (amortized)
20k dataset			
Rot. (\downarrow)	2e-4	1.7	5e-4
Trans. (\downarrow)	8.7	10.9	1.4
Res. (\downarrow)	2.14/2.14	4.82/4.04	2.61/2.63
Err. (\downarrow)	0%	38%	0.01%
100k dataset			
Rot. (\downarrow)	2e-4	5e-4	3e-4
Trans. (\downarrow)	5.7	9.7	0.9
Res. (\downarrow)	2.03/2.06	2.64/2.61	2.54/2.55
Err. (\downarrow)	0.07%	0.02%	0.009%


 Figure 3: Distributions of predicted conformations along the PC1 axis for the 20k (**top**) and 100k (**bottom**) 80S-bimodal datasets.

of ground-truth conformations increase, narrower z value distributions around cluster centers become much more beneficial (see 1D-motion dataset benchmark results below).

Benchmark on the 1D-motion dataset

The 1D-motion dataset consists of 10 distinct conformations, presenting a challenging task for conformation classification. The benchmark results are shown in Table 2 and Figure 5. Besides the pose (rotation and translation) error, we quantified the classification accuracy using the Spearman correlation coefficient (**Corr.**) between the ground-truth labels and the projections of latent- z along the first principal component PC1. HetACUMN outperformed cryoDRGN2 and cryoFIRE in all metrics. Since there are equal number of images for the 10 ground-truth classes, we expect the latent- z for each class to be similarly distributed around the probability density peak values. A closer look revealed that these distributions are quite uneven for cryoDRGN2 and cryoFIRE ((Figure 5). Especially for the last several classes, the distribution estimated by cryoFIRE become some degenerate peaks that cannot be distinguish between

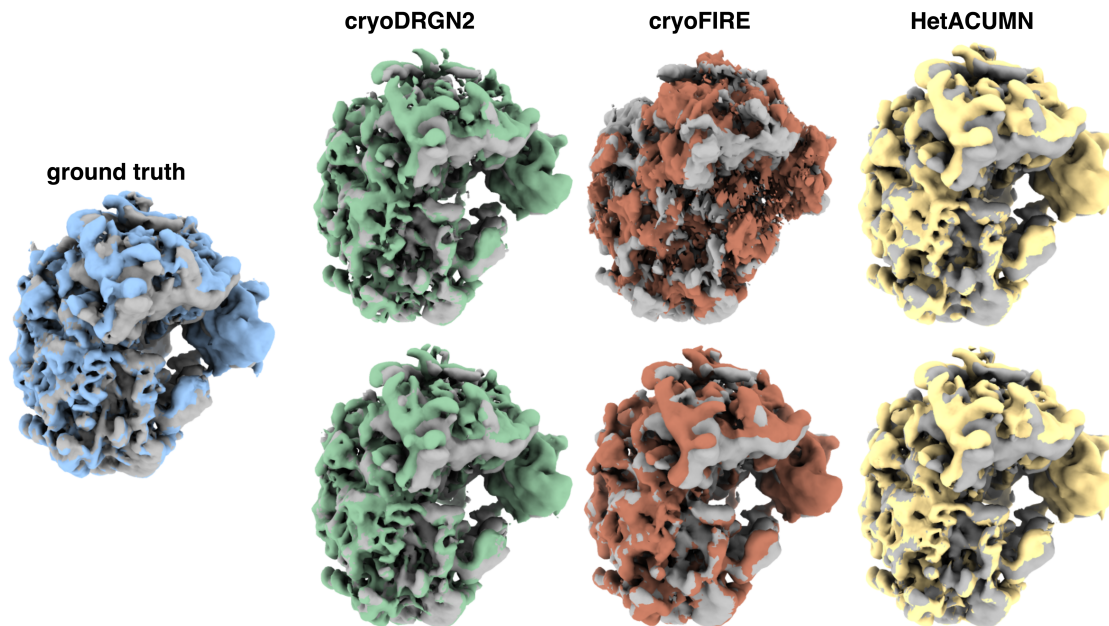


Figure 4: Visualization of the ground-truth volumes and predicted volumes from cryoDRGN2, cryoFIRE, and HetACUMN, reconstructed from the 20k (**top**) and 100k (**bottom**) 80S-bimodal datasets. The two conformational states are superposed with one state shown in color and the other in grey.

them. In contrast, the shapes of the latent- z distribution for HetACUMN are similar and distinguishable regardless of the underlying conformation class.

In addition, we generated visualization of the volumes of the 1st, 5th, and 10th classes from cryoDRGN2, HetACUMN, and the ground truth (see Figure 6). Comparing with the ground truth, it is no obvious difference for cryoDRGN2 and cryoFIRE on the first two volumes. But for the 10th class, there is some visible inconsistency of predicted volume against the ground truth. This observation is consistent with the latent- z distribution mentioned above.

Table 2: Benchmark results for the 1D-motion dataset (100k).

Method	cryoDRGN2	cryoFIRE	HetACUMN
Rot. (\downarrow)	8e-3	2e-2	7e-3
Trans. (\downarrow)	4.3	5.4	3.1
Corr. (\uparrow)	0.963	0.951	0.976

Latent-space Entanglement

Using the metric defined in Eq. 11, here we quantitatively compare the latent-space entanglement of cryoDRGN2, cryoFIRE, and HetACUMN. For all three datasets (bimodal 20k, bimodal 100k, 1D motion), HetACUMN showed the least entanglement of the latent space for pose and conformation, and outperformed cryoFIRE by a significant amount. It is worth noting that cryoDRGN2 estimates the poses through search-based algorithms rather than using a neural network. This design makes cryoDRGN2 less prone to latent-space entanglement than cryoFIRE. The fact that HetACUMN performed still better than cryoDRGN2 demonstrates the value of adding the conditional pose prediction task during training.

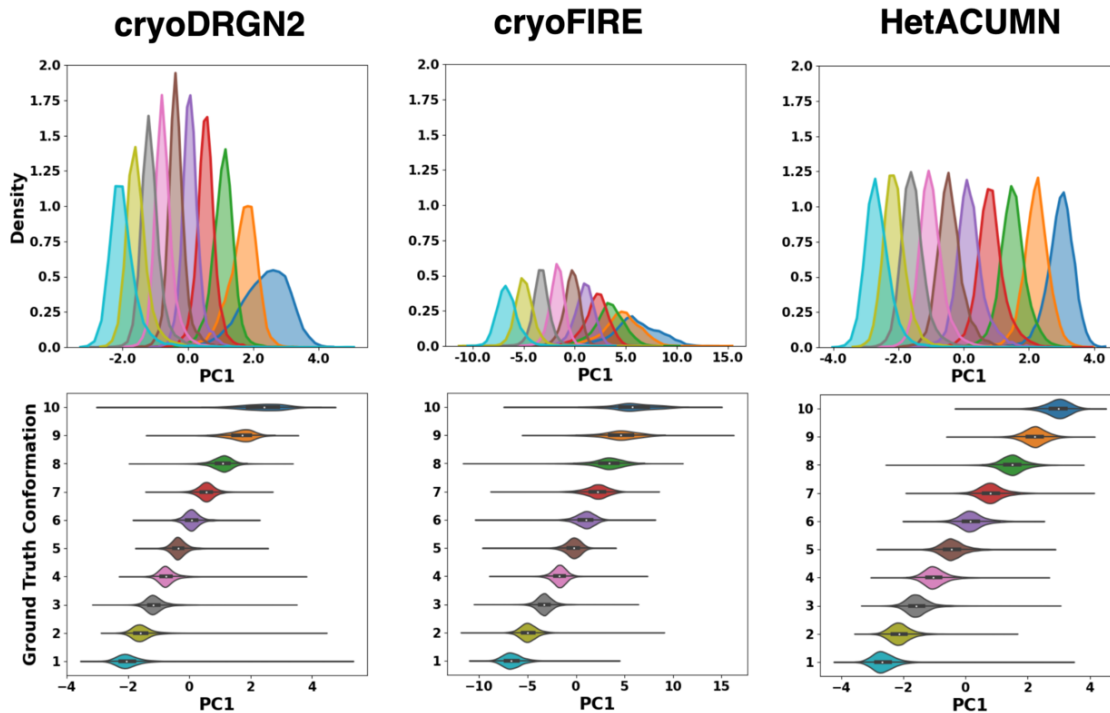


Figure 5: Distribution of the latent- z for benchmark tests on the 1D-motion dataset (100k). (a) probability density distribution of the latent- z along the PC1 axis after dimension reduction.; (b) violin plots for the latent- z statistics for each class.

Table 3: Entanglement $E_{entangle}$ (\downarrow) for all three methods.

Methods	cryoDRGN2	cryoFIRE	HetACUMN
bimodal 20k	7.3e-4	2.08	6.8e-4
bimodal 100k	1.2e-3	1.3e-3	4.4e-4
1D motion	4.6e-2	8.2e-2	1.0e-2

5.2 Reconstructions on an Experimental Dataset

Experimental Setup

To test the applicability of HetACUMN on real experimental cryo-EM data, we chose the precatalytic spliceosome dataset from the EMPIAR database (ID: EMPIAR-10180) [14, 13], which was downsampled to an image size of $D = 128$ (4.2475 Å/pixel). We run HetACUMN with the same training settings as for the simulated datasets.

Performance

For experimental datasets, the distribution of noise is often more complex than simulated datasets. Based on our simplified noise estimation method (Equation 9), the SNR of spliceosome datasets is around -11.7 dB, which is worse than the simulated datasets above. We predicted the latent z for the full dataset, then sampled three points along the first component axis and generated the corresponding volumes. As shown in Figure 7, changes in the shape of the reconstructed volumes indicate a large flexible motion in the continuous conformational space. The corresponding predicted volumes and the distribution of predicted latent z along the first two principal component axes are similar to that from the literature [30].

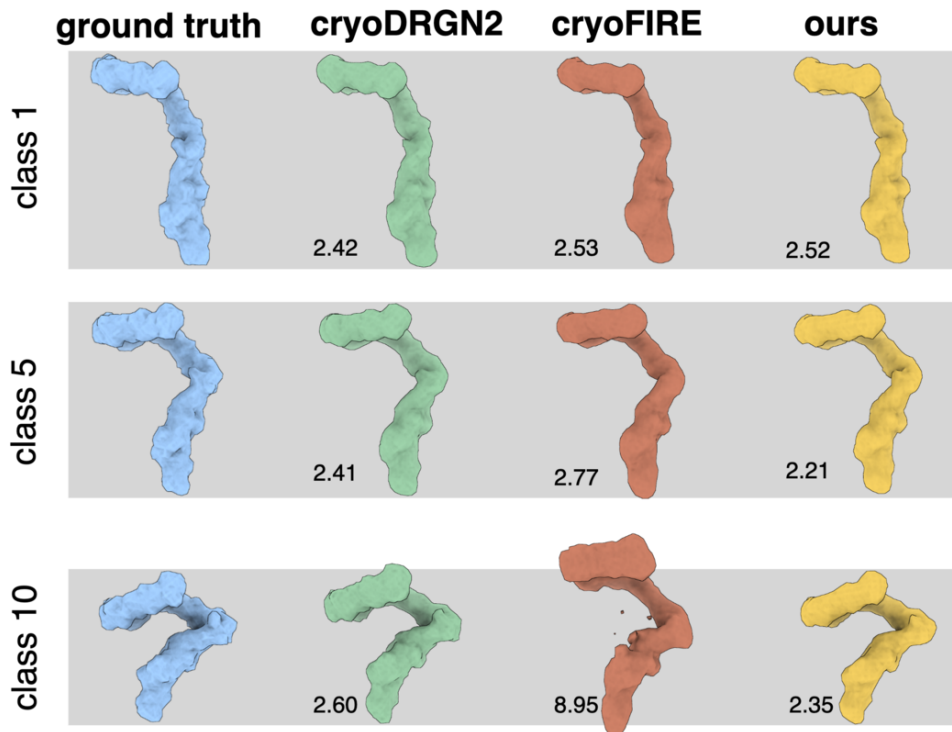


Figure 6: Visualization of the ground-truth and predicted volumes for the 1st, 5th, and 10th conformational classes, reconstructed from the 1D-motion dataset (100k). FSC resolutions (in pixels) are shown at the lower left corners.

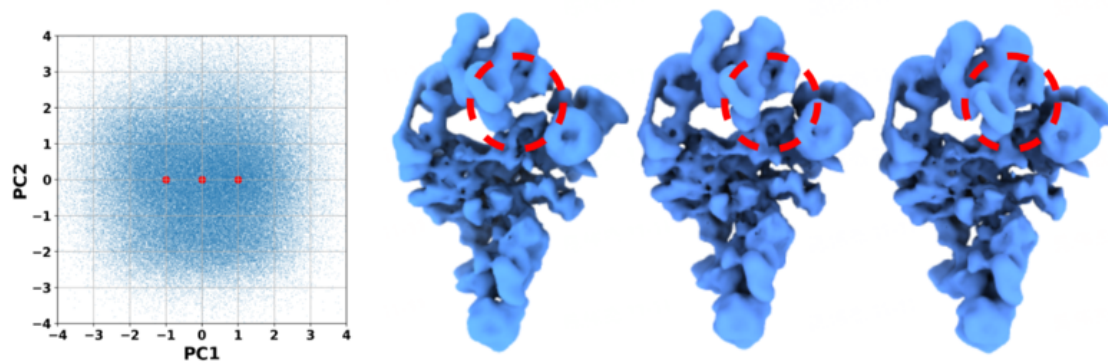


Figure 7: Visualization of the latent conformation space and volumes predicted by HetACUMN using the spliceosome dataset (EMPIAR-10180) from real experiments. Three representative volumes are shown here, sampled along the PC1 axis (PC1 values from left to right: -1, 0, 1)

6 Ablation Study

As mentioned in section 4, we proposed a novel training task **CPP** to explicitly enforce the disentanglement of conformation state and pose. Besides, HetACUMN also uses three strategies to improve the performance of pose estimations and conformation classifications.

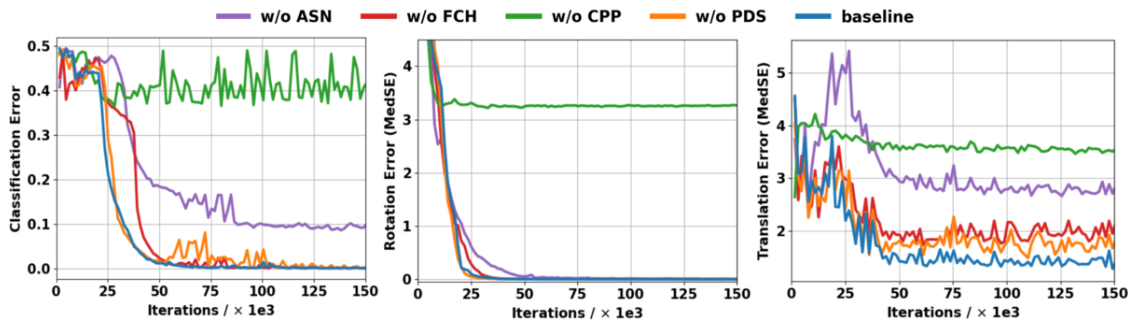


Figure 8: Ablation study for HetACUMN benchmarked on the 80S-bimodal dataset (20k).

- **Frozen Conformation-prediction Head (FCH)**: Both cryoFIRE [9] and HetACUMN freeze the conformation-prediction head during the early training stage in order to mitigate the difficulties of the volume generation and pose estimation.
- **Posterior z -Distribution Sampling (PDS)**: To generate synthetic images, we sampled conformational states z from the posterior distribution $q(z|\mathcal{I})$ instead of the prior distribution $p(z)$ (i.e., the standard Gaussian distribution).
- **Adaptive Synthetic Noise (ASN)**: in the CPP task, we generated adaptive noise using a fixed SNR instead of a fixed noise variance.

To quantify the necessity of the CPP task as well as the three strategies mentioned above, we designed four ablation experiments using the 80S-bimodal (20k) dataset, while keeping other training setup unchanged. HetACUMN with a full setup was used as the baseline.

As shown in Figure 8, without the CPP task, large errors in conformation classifications and pose estimations are observed. One explanation is that conformational states and poses are both latent variables without direct supervision. It is difficult to learn their corresponding physical meaning through indirect supervision with an image reconstruction loss especially during the early training phase. This difficulty has also been observed in other studies [19]. The CPP task adds direct supervision to the pose variable, making it disentangled from the conformational state variable.

In addition to the CPP task, other strategies also contribute to reducing estimation errors (Figure 8). For image translation estimation, all three strategies (FCH, PDS, and ASN) are necessary. For conformation classification, ASN appears to be critical. During the early training phase, without ASN, extremely strong noise can overwhelm the signal of images and mislead the encoder. Both FCH and PDS helped to reduce the estimation instabilities. For rotation (orientation) estimation, the absence of ASN and FCH slightly delayed the convergence while removing PDS seemed to have little effect. Therefore, we recommend using the full setup when employing HetACUMN for heterogeneous cryo-EM reconstruction tasks.

7 Conclusions

In this paper, we discuss the challenges of heterogeneous cryo-EM reconstruction, including low signal-to-noise ratio, unknown poses, and complex distributions of underlying 3D structures.

To address these challenges, we propose a self-supervised deep learning framework called HetACUMN based on amortized inference. By alternating the variational image reconstruction task and the conditional pose prediction task, the VAE-based architecture explicitly enforces the disentanglement of the conformation and pose latent space. The experiments on simulated datasets show that HetACUMN outperformed other amortized-inference-base methods like cryoFIRE. On the other hand, our method has comparable accuracy of pose estimation and even better performance in estimating conformational distribution than non-amortized methods. Furthermore, we demonstrated that HetACUMN can also be used on experimental datasets.

There are still some limitations of our method. For example, the latent z space is capable of representing significant amounts of conformational variations. However, real experimental datasets is often complex and the reduced z space through principal component analysis may not be the best choice for conformational classification. Further study in this direction is needed.

Overall, we believe there is a great potential in applying deep learning approaches for heterogeneous cryo-EM reconstruction. It provides a new path for improving the accuracy and efficiency of this challenging task.

References

- [1] Claire Donnat, Axel Levy, Frédéric Poitevin, Ellen D. Zhong, and Nina Miolane. Deep generative modeling for volume reconstruction in cryo-electron microscopy. *Journal of Structural Biology*, 214:107920, 2022.
- [2] Rachel-Ann A Garibhsingh, Elias Ndaru, Alisa A Garaeva, Yueyue Shi, Laura Zielewicz, Paul Zakrepine, Massimiliano Bonomi, Dirk J Slotboom, Cristina Paulino, Christof Grewer, et al. Rational design of asct2 inhibitors using an integrated experimental-computational approach. *Proceedings of the National Academy of Sciences (USA)*, 118(37):e2104093118, 2021.
- [3] Harshit Gupta, Michael T. McCann, Laurène Donati, and Michael Unser. Cryogan: A new reconstruction paradigm for single-particle cryo-em via deep adversarial learning. *IEEE Transactions on Computational Imaging*, 7:759–774, 2021.
- [4] Mohamad Harastani, Mikhail Eltsov, Amélie Leforestier, and Slavica Jonic. Hemmma-3d: Cryo electron tomography method based on normal mode analysis to study continuous conformational variability of macromolecular complexes. *Frontiers in Molecular Biosciences*, 8, 2021.
- [5] Kaiming He, Xiangyu Zhang, Shaoqing Ren, and Jian Sun. Deep residual learning for image recognition. In *Proceedings of the IEEE conference on computer vision and pattern recognition*, pages 770–778, 2016.
- [6] David Herreros, Roy R. Lederman, James Krieger, Amaya Jiménez-Moreno, Marta Martínez, David Myška, David Strelak, Jiri Filipovic, Ivet Bahar, Jose Maria Carazo, and Carlos Oscar S. Sanchez. Approximating deformation fields for the analysis of continuous heterogeneity of biological macromolecules by 3D Zernike polynomials. *IUCrJ*, 8:992–1005, 2021.
- [7] Roy R Lederman, Joakim Andén, and Amit Singer. Hyper-molecules: on the representation and recovery of dynamical structures for applications in flexible macro-molecules in cryo-em. *Inverse Problems*, 36:044005, 2020.
- [8] A. Levy, F. Poitevin, J. Martel, Y. Nashed, A. Peck, N. Miolane, D. Ratner, M. Dunne, and G. Wetzstein. CryoAI: Amortized Inference of Poses for Ab Initio Reconstruction of 3D Molecular Volumes from Real Cryo-EM Images. In *European Conference on Computer Vision (ECCV)*, 2022.
- [9] Axel Levy, Gordon Wetzstein, Julien N.P Martel, Frederic Poitevin, and Ellen Zhong. Amortized inference for heterogeneous reconstruction in cryo-em. In S. Koyejo, S. Mohamed, A. Agarwal, D. Belgrave, K. Cho, and A. Oh, editors, *Advances in Neural Information Processing Systems*, volume 35, pages 13038–13049, 2022.
- [10] Roberto Marabini, Steven J Ludtke, Stephen C Murray, Wah Chiu, M Jose, Ardan Patwardhan, J Bernard Heymann, and Jose M Carazo. The electron microscopy exchange (emx) initiative. *Journal of structural biology*, 194(2):156–163, 2016.
- [11] Youssef S. G. Nashed, Frédéric Poitevin, Harshit Gupta, Geoffrey Woollard, Michael Kagan, Chun Hong Yoon, and Daniel Ratner. Cryoposenet: End-to-end simultaneous learning of single-particle orientation and 3d map reconstruction from cryo-electron microscopy data. In *Proceedings of the IEEE/CVF International Conference on Computer Vision (ICCV) Workshops*, pages 4066–4076, October 2021.
- [12] Nobel. The Nobel Prize in Chemistry 2017, 2017.
- [13] C Plaschka, PC Lin, K Nagai, T Nakane, D Kimanius, E Lindahl, and SHW Scheres. EMPIAR-10180. <https://www.ebi.ac.uk/empiar/EMPIAR-10180>, 2018.
- [14] Clemens Plaschka, Pei-Chun Lin, and Kiyoshi Nagai. Structure of a pre-catalytic spliceosome. *Nature*, 546:617—621, 2017.
- [15] Ali Punjani and David Fleet. 3d flexible refinement: Structure and motion of flexible proteins from cryo-em. *Microscopy and Microanalysis*, 28:1218—1218, 2022.
- [16] Ali Punjani and David J Fleet. 3D variability analysis: Resolving continuous flexibility and discrete heterogeneity from single particle cryo-em. *Journal of structural biology*, 213:107702, 2021.
- [17] A. Punjani, J. L. Rubinstein, D. J. Fleet, and M. A. Brubaker. cryosparc: algorithms for rapid unsupervised cryo-em structure determination. *Nature Methods*, 14(3):290–296, 2017.
- [18] Ali Rahimi and Benjamin Recht. Random features for large-scale kernel machines. *Advances in neural information processing systems*, 20, 2007.
- [19] Dan Rosenbaum, Marta Garnelo, Michal Zielinski, Charlie Beattie, Ellen Clancy, Andrea Huber, Pushmeet Kohli, Andrew W. Senior, John Jumper, Carl Doersch, S. M. Ali Eslami, Olaf Ronneberger, and Jonas Adler. Inferring a continuous distribution of atom coordinates from cryo-em images using vaes. *CoRR*, abs/2106.14108, 2021.
- [20] Sjors H.W. Scheres. Relion: Implementation of a bayesian approach to cryo-em structure determination. *Journal of Structural Biology*, 180:519–530, 2012.
- [21] Sjors HW Scheres. Relion: implementation of a bayesian approach to cryo-em structure determination. *Journal of structural biology*, 180(3):519–530, 2012.
- [22] M. Shekhar, G. Terashi, C. Gupta, G. Debussche, N. J. Sisco, J. Nguyen, J. Zook, J. Vant, D. Sarkar, and P. Fromme. Cryofold: Ab-initio structure determination from electron density maps using molecular dynamics. *Cold Spring Harbor Laboratory*, 2019.
- [23] Amit Singer and Fred J. Sigworth. Computational methods for single-particle electron cryomicroscopy. *Annual Review of Biomedical Data Science*, 3(1):163–190, 2020.
- [24] Matthew Tancik, Pratul Srinivasan, Ben Mildenhall, Sara Fridovich-Keil, Nithin Raghavan, Utkarsh Singhal, Ravi Ramamoorthi, Jonathan Barron, and Ren Ng. Fourier features let networks learn high frequency functions in low dimensional domains. *Advances in Neural Information Processing Systems*, 33:7537–7547, 2020.

- [25] Karen Ullrich, Rianne van den Berg, Marcus A. Brubaker, David J. Fleet, and Max Welling. Differentiable probabilistic models of scientific imaging with the Fourier slice theorem. In *Proceedings of The 35th Uncertainty in Artificial Intelligence Conference, PMLR*, 2020.
- [26] Miloš Vulović, Raimond BG Ravelli, Lucas J van Vliet, Abraham J Koster, Ivan Lazić, Uwe Lücken, Hans Rullgård, Ozan Öktem, and Bernd Rieger. Image formation modeling in cryo-electron microscopy. *Journal of structural biology*, 183(1):19–32, 2013.
- [27] Wilson Wong, Xiao-chen Bai, Alan Brown, Israel S Fernandez, Eric Hanssen, Melanie Condron, Yan Hong Tan, Jake Baum, and Sjörs HW Scheres. Cryo-em structure of the plasmodium falciparum 80s ribosome bound to the anti-protozoan drug emetine. *Elife*, 3:e03080, 2014.
- [28] Lin Yao, Ruihan Xu, Zhifeng Gao, Guolin Ke, and Yuhang Wang. Boosted ab initio cryo-em 3d reconstruction with ace-em, 2023.
- [29] Gang Ye, Bin Liu, and Fang Li. Cryo-em structure of a sars-cov-2 omicron spike protein ectodomain. *Nature communications*, 13:1214, 2022.
- [30] Ellen D Zhong, Tristan Bepler, Bonnie Berger, and Joseph H Davis. Cryodrgn: reconstruction of heterogeneous cryo-em structures using neural networks. *Nature methods*, 18(2):176–185, 2021.
- [31] Ellen D. Zhong, Tristan Bepler, Bonnie Berger, and Joseph H. Davis. Data for "CryoDRGN: Reconstruction of heterogeneous cryo-EM structures using neural networks" doi: 10.5281/zenodo.4355284, Jan. 2021.
- [32] Ellen D. Zhong, Tristan Bepler, Joseph H. Davis, and Bonnie Berger. Reconstructing continuous distributions of 3d protein structure from cryo-em images. In *International Conference on Learning Representations*, 2019.
- [33] Ellen D. Zhong, Adam Lerer, Joseph H. Davis, and Bonnie Berger. Cryodrgn2: Ab initio neural reconstruction of 3d protein structures from real cryo-em images. In *2021 IEEE/CVF International Conference on Computer Vision (ICCV)*, pages 4046–4055, 2021.

A Model architecture

A1 Encoder

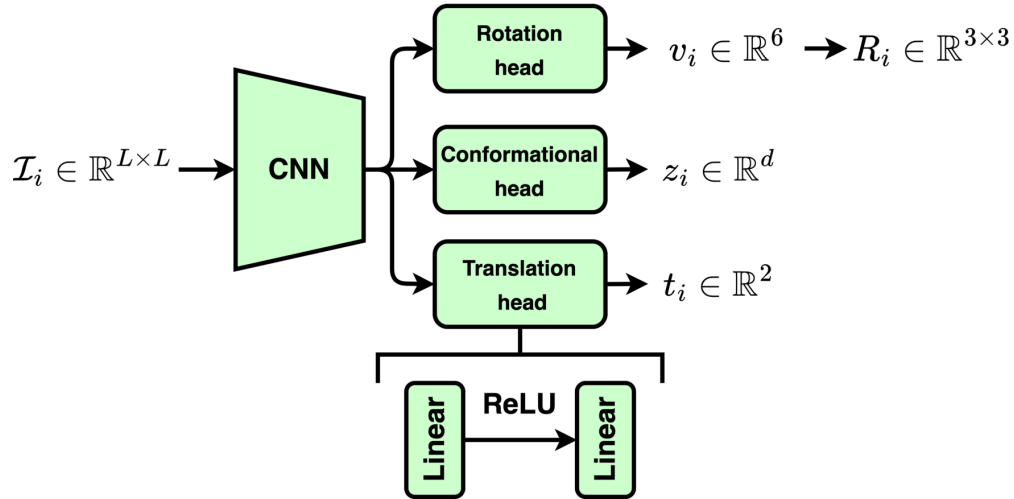


Figure S1: Architecture of the encoder.

Figure S1 shows the architecture of the HetACUMN encoder. The architecture of Convolutional Neural Network (CNN) is the same as the standard ResNet-18 [5] without the full connection layer. The output of CNN is flattened and fed into three parallel fully connected neural networks with a hidden layer dimension of 256.

A2 Decoder

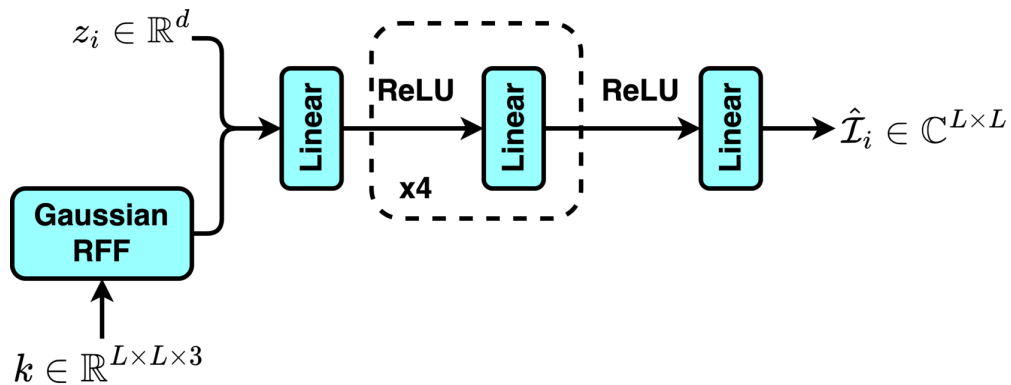


Figure S2: Architecture of the decoder.

Figure S2 shows the architecture of the HetACUMN decoder. The Fourier-space coordinates $k \in \mathbb{R}^{L \times L \times 3}$ are encoded by the Gaussian random Fourier Features (RFF) mapping [18, 24]. Then, the conformational state z_i and encoded coordinates are fed into the coordinate-based fully connected neural networks with a hidden layer dimension of 256.

B Dataset preparation

Simulated datasets

The simulated datasets were created from ground-truth volumes using the forward cryo-EM image formation model as described in the main text. Each ground-truth volume was first rotated to a certain orientation sampled uniformly from the 3D rotation group $SO(3)$. A projection image was formed by integrating the voxel values along z axis (orthogonal to the projection plane). CTF effects were added to the projection image with CTF parameters uniformly from the experimental dataset EMPIAR-10028. Then, Gaussian noise was added to the projection image to reach an SNR of -10 dB. Finally, a random 2D image translation was added which was sampled from a uniform distribution within the range of $[-8, 8]$ pixels.

For the “80S-bimodal” dataset, the two ground-truth volumes (rotated and un-rotated states of the 80S ribosome protein) were selected from a previous published dataset [30, 31]. Each volume has a cubic shape with edge length $D = 128$. The generated projection image has a pixel size of $3.77 \text{ \AA}/\text{pixel}$. As for the “1D-motion” dataset, the protein fragment (residues 177–330 from chain A with hydrogen atoms removed) was taken from a published atomic structure of the ASCT2 protein (PDB ID: 7BCQ) [2]. The 1D rigid-body motion was generated by rotating atoms around the backbone C-CA bond of residue GLY249 (see Figure S7). The rotation angles were taken from the following sequence $\{9^\circ, 18^\circ, \dots, 90^\circ\}$.

Experimental dataset

The precatalytic spliceosome experimental dataset was downloaded from the EMPIAR database (ID: EMPIAR-10180) [13, 14]. The original dataset was filtered to a final size of 139,722 images using the indices from a previous study [31] and downsampled to an image size of $D = 128$ and a pixel size of $4.2475 \text{ \AA}/\text{pixel}$. Since the raw images were significantly off-centered, all images were recentered using the published image translation values [14].

C Performance with time constraints

For real-world applications, cryo-EM data analyses are often subject to time constraints, especially in industrial settings. Therefore, it is important to consider the performance within a given wall-clock time. Here we show the performance of cryoDRGN2, cryoFIRE, and HetACUMN within a wall-clock time of 30 hours (Figure S3). For all three datasets, HetACUMN achieved similar or better performance compared to cryoDRGN2 and cryoFIRE in terms of classification performance, rotation error (mean and median), and translation error (mean and median). Note that Table 1 and 2 in the main text report the best performance after reaching convergence in classification performance, not necessarily at the end of training shown here.

D FSC resolution analysis

To quantify the volume reconstruction quality of the three methods, we performed Fourier shell correlation (FSC) analysis for all predicted volumes against the ground-truth volumes. Each volume was generated based on a representative classification latent vector z_i^* for images of the corresponding ground-truth conformational class i . To calculate z_i^* , we first performed PCA dimension reduction for all z vectors of the same ground-truth conformational class i . Then, we projected these vectors along the first principal component (PC1) and selected the z corresponding to the highest probability density of this 1D z -distribution (see Figure 3 and 5 in the main text). Following the convention in the field of cryo-EM, the resolutions of the predicted volumes were estimated at an FSC cutoff of 0.5, i.e., the spatial frequency at which the FSC curve drops to 0.5. As a common practice, the resolutions reported here are expressed in terms of the inverse of the spatial frequencies. As a result, the lower the value, the better the resolution.

Figure S4 shows the FSC analysis for the two 80S bimodal datasets. When using the 80S bimodal 20k dataset, the resolution of the reconstructed volumes from cryoDRGN2 and HetACUMN are similar. However, the volume reconstructed by cryoFIRE showed much lower resolutions. When using the 100k 80S bimodal dataset, all three methods achieved similar reconstruction quality.

For the 1D-motion dataset, HetACUMN achieved better resolutions compared to cryoDRGN2 for all 10 conformational classes except for class 1. On the other hand, the resolutions of the volumes reconstructed by cryoFIRE were lower than both cryoDRGN2 and HetACUMN, and gradually deteriorated from class 1 to class 10 (Figure S5). For easier cross-comparison, we also plotted the distribution of the FSC resolutions for all 10 conformational classes (Figure S6). Lastly, we show the visualization of the reconstructed volumes for all 10 conformation classes (Figure S7).

E Comparison on experimental datasets

The performance of HetACUMN is comparable to cryoDRGN2 and cryoFIRE on the experimental dataset (Figure S8). Note that a precise cross-method comparison cannot be done because of the lack of ground-truth labels in real-world cryo-EM experiments.

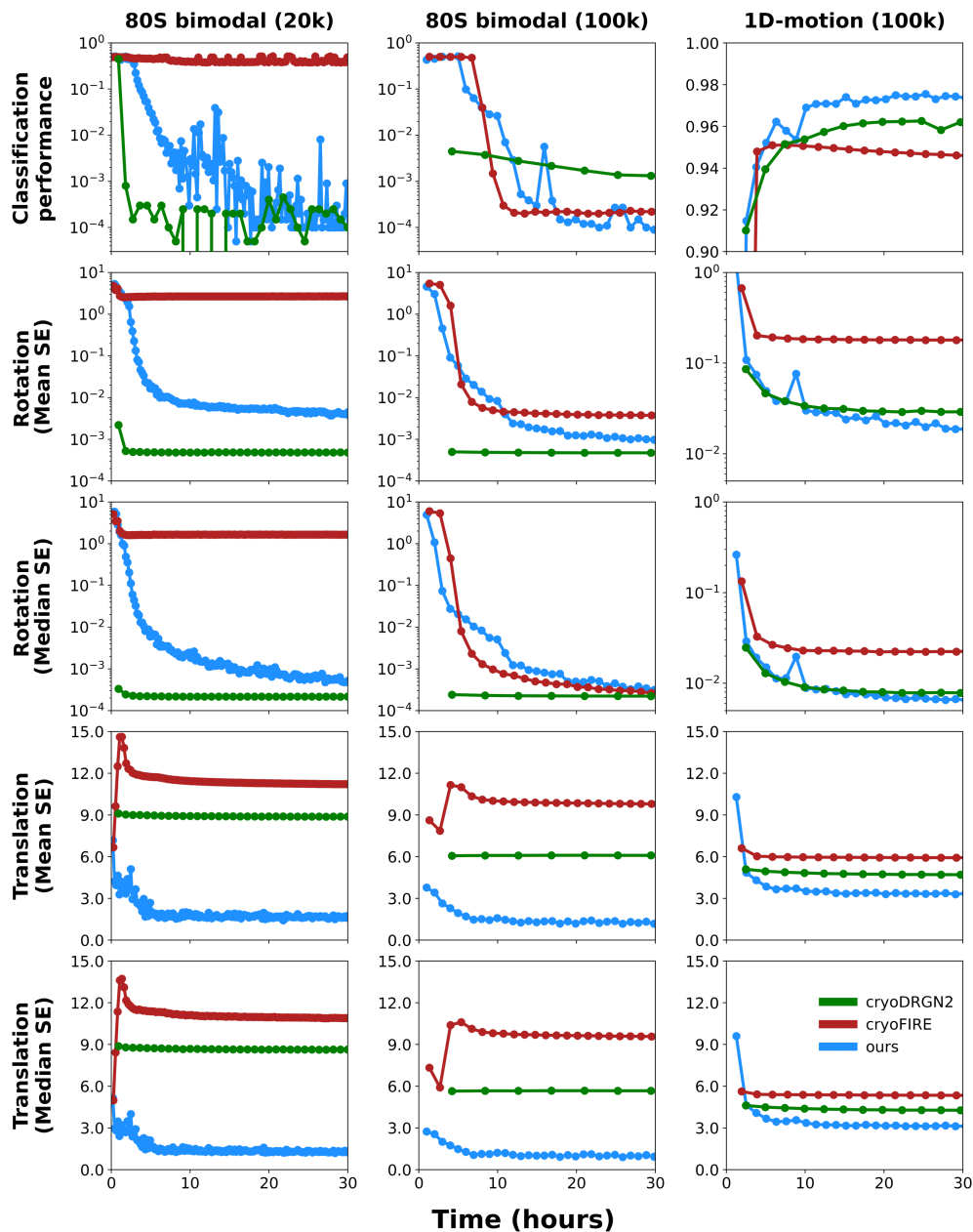


Figure S3: The performance of cryoDRGN2 (green), cryoFIRE (red), and HetACUMN (blue) within a wall-clock time of 30 hours, which were benchmarked on three datasets (left to right): 80S bimodal (20k), 80S bimodal (100k), 1D-motion (100k). The classification performance was quantified in terms of confusion error (\downarrow) for the two 80S bimodal datasets or Spearman correlation coefficient (\uparrow) for the 1D-motion dataset. The rotation error (\downarrow) is defined as the Frobenius norm of the difference matrix between the ground-truth and predicted rotation matrices. The translation error (\downarrow) is defined as the L2 norm of the difference vector (in pixels) between the ground-truth and predicted translation vectors. Both mean and median squared errors (SE) for rotation and translation are reported here.

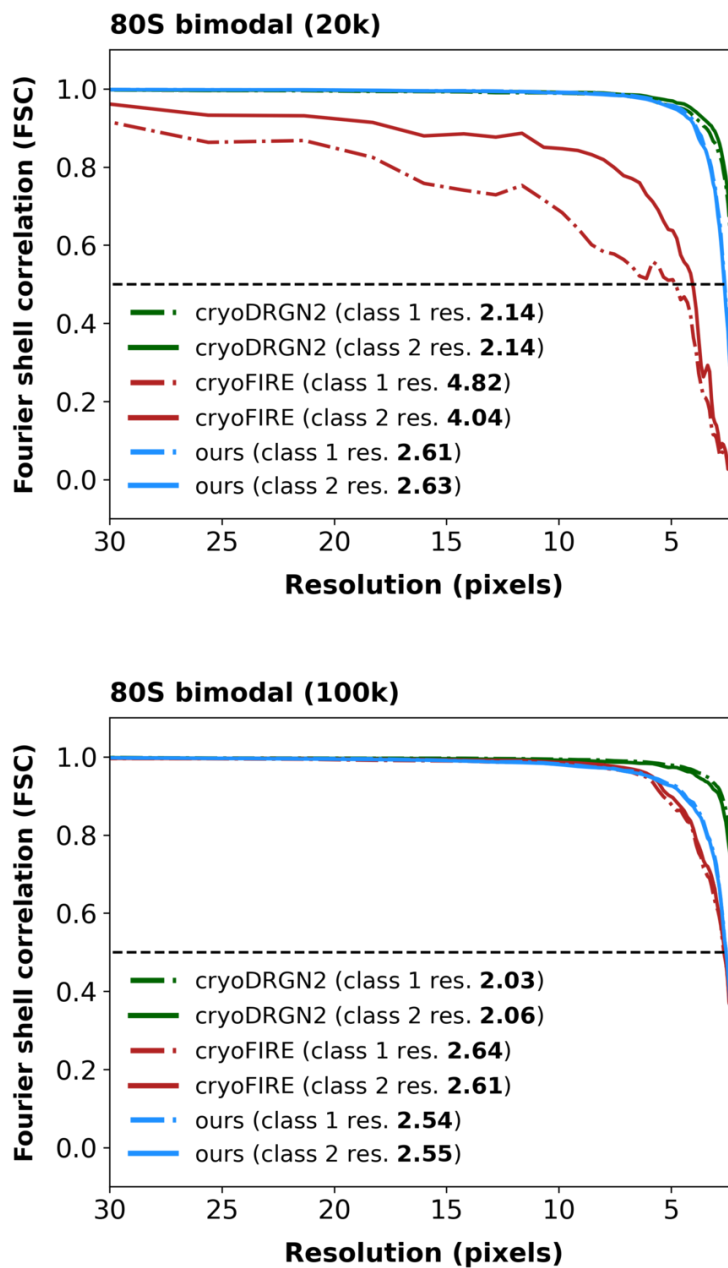


Figure S4: Fourier shell correlation (FSC) analysis for the predicted vs. ground-truth volumes of both conformational classes from the 20k (**top**) and 100k (**bottom**) 80S bimodal datasets. Resolutions (res.) in pixels of the predicted volumes are estimated at an FSC cutoff of 0.5 (dashed line) and marked in **bold** text.

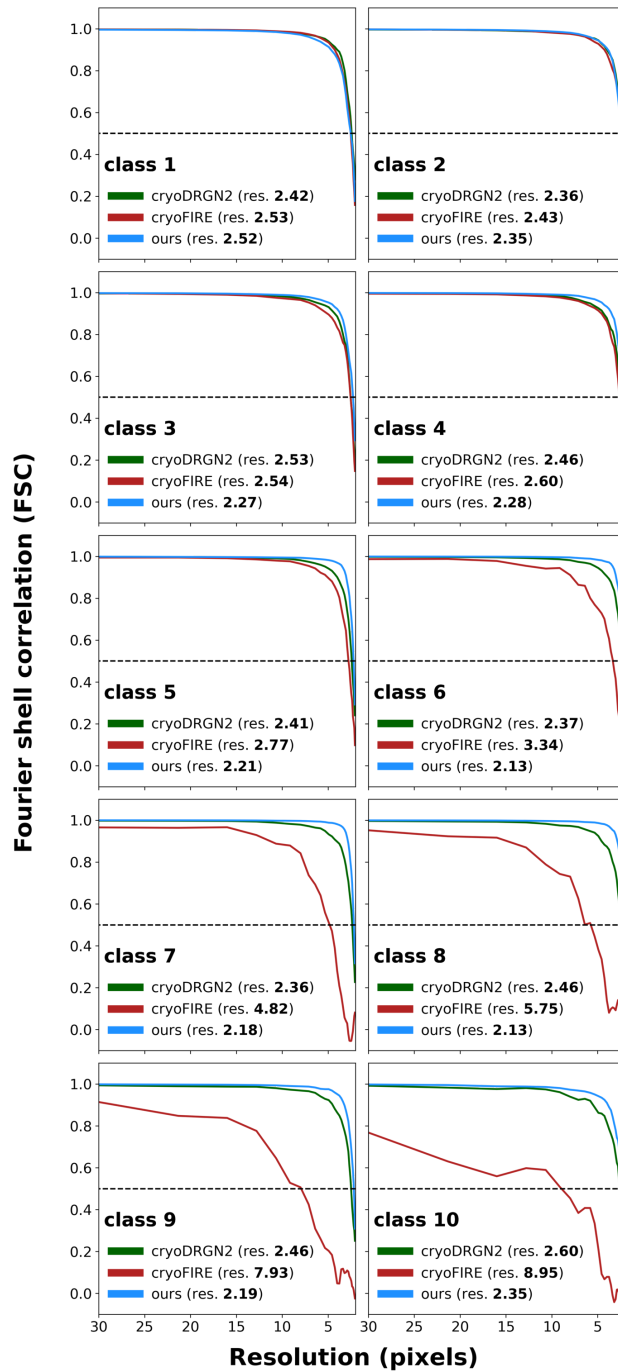


Figure S5: Fourier shell correlation (FSC) analysis for the predicted vs. ground-truth volumes of each conformational class from the 1D-motion dataset. Resolutions (res.) in pixels of the predicted volumes are estimated at the FSC cutoff of 0.5 (dashed line) and marked in **bold** text.

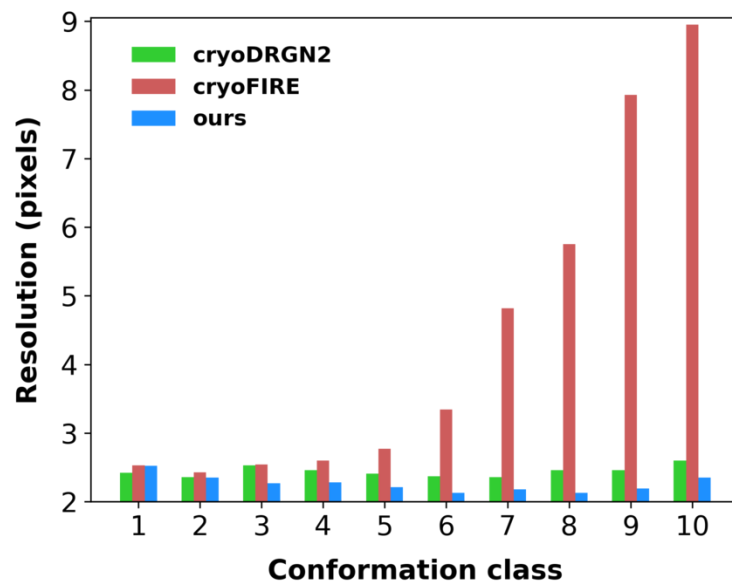


Figure S6: Distribution of the FSC resolutions in pixels (a lower value means better resolution) for volumes from all 10 conformational classes of the 1D-motion dataset generated by cryoDRGN2, cryoFIRE, and HetACUMN.

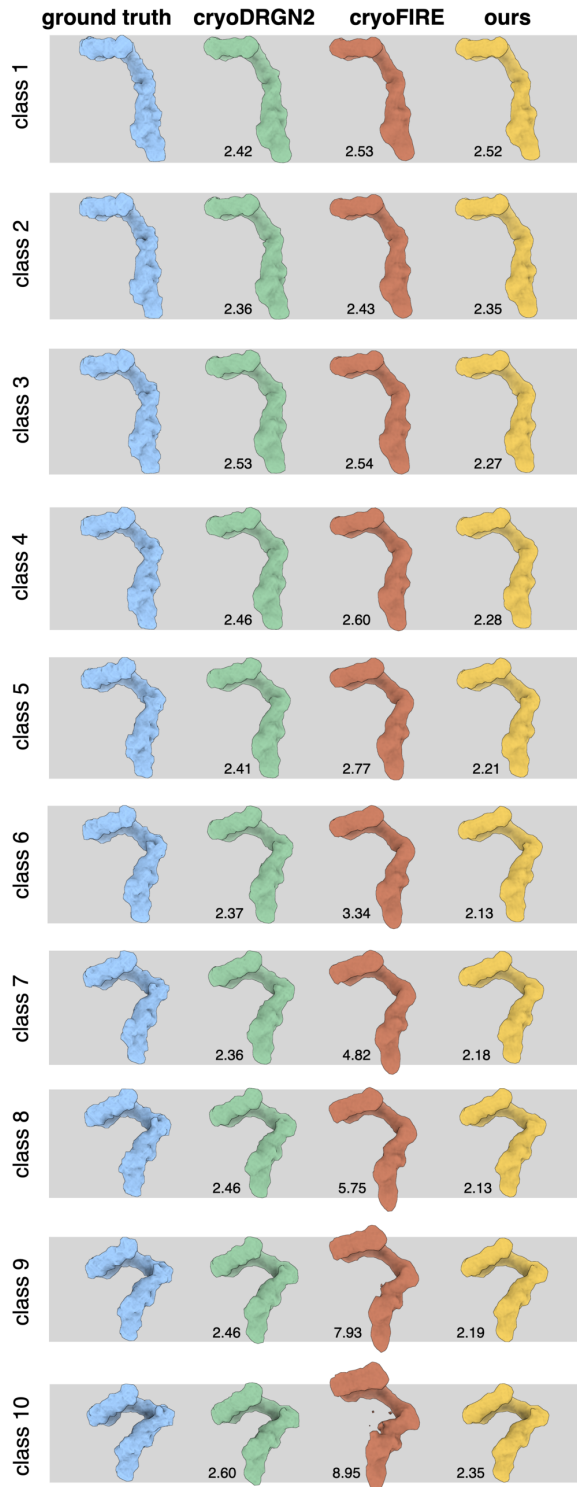


Figure S7: Visualization of the ground-truth and predicted volumes of the 10 conformational classes in the 1D-motion dataset. FSC resolutions (in pixels) are shown at the lower left corners. The gray boxes serve as visualization aids for easier comparison. Their heights are adjusted to precisely fit the ground-truth volumes. **Top to bottom**: conformational class 1 to 10. **Left to right**: ground truth, cryoDRGN2, cryoFIRE, and HetACUMN (ours).

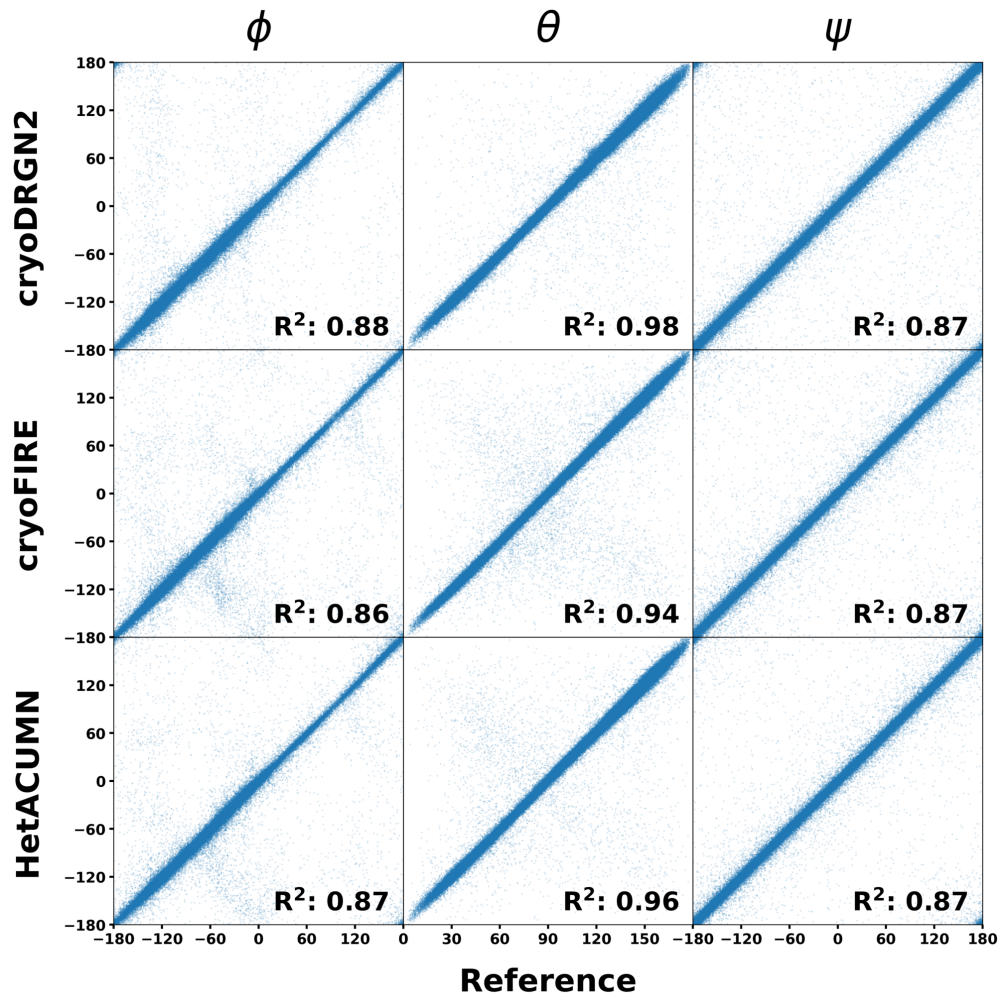


Figure S8: Comparison of the Euler angles between the published reference and the predictions for the experimental spliceosome dataset. R^2 values are shown in bold.